TOPICAL REVIEW — Plasmonics and metamaterials

Manipulation of plasmonic wavefront and light–matter interaction in metallic nanostructures: A brief review*

Li Jia-Fang(李家方)† and Li Zhi-Yuan(李志远)‡

Laboratory of Optical Physics, Institute of Physics, Chinese Academy of Sciences, Beijing 100190, *China*

(Received 27 November 2013; revised manuscript received 24 December 2013; published online 20 March 2014)

The control and application of surface plasmons (SPs), is introduced with particular emphasis on the manipulation of the plasmonic wavefront and light–matter interaction in metallic nanostructures. We introduce a direct design methodology called the surface wave holography method and show that it can be readily employed for wave-front shaping of near-infrared light through a subwavelength hole, it can also be used for designing holographic plasmonic lenses for SPs with complex wavefronts in the visible band. We also discuss several issues of light–matter interaction in plasmonic nanostructures. We show theoretically that amplification of SPs can be achieved in metal nanoparticles incorporated with gain media, leading to a giant reduction of surface plasmon resonance linewidth and enhancement of local electric field intensity. We present an all-analytical semiclassical theory to evaluate spaser performance in a plasmonic nanocavity incorporated with gain media described by the four-level atomic model. We experimentally demonstrate amplified spontaneous emission of SP polaritons and their amplification at the interface between a silver film and a polymer film doped with dye molecules. We discuss various aspects of microscopic and macroscopic manipulation of fluorescent radiation from gold nanorod hybrid structures in a system of either a single nanoparticle or an aligned group of nanoparticles. The findings reported and reviewed here could help others explore various approaches and schemes to manipulate plasmonic wavefront and light–matter interaction in metallic nanostructures for potential applications, such as optical displays, information integration, and energy harvesting technologies.

Keywords: surface plasmons, surface wave holography, surface plasmon amplification, fluorescence enhancement, gold nanorods

PACS: 73.20.Mf, 41.20.Jb, 78.67.–n, 42.60.Da **DOI:** 10.1088/1674-1056/23/4/047305

1. Introduction

Surface plasmons (SPs) carry information or energy that can be localized around or transported among nanoscale metallic structures without suffering from the diffraction limits of light. Therefore, the manipulation of SPs is fundamental for the potential applications of plasmonics.

Surface plasmons are coherent electron oscillations that are confined at a metal–dielectric interface. Depending on the geometry of the interface, SPs can propagate along or be localized around the interface, two cases which are usually called, respectively, propagating SPs (or surface plasmon polaritons, SPPs) and localized SPs. When the frequency of light matches the natural frequency of collective electron oscillations on the metal–dielectric interface with respect to the positive nuclei, surface plasmon resonance (SPR) will be excited.[1–3] The interaction of photons with SPs is then significantly enhanced, leading to a great enhancement of local electric field intensity and sensitivity of plasmonic mode response to environment. For example, a direct consequence of local-field enhancement is that, when molecules located on metal nanoparticles are excited by incident light, their fluorescence or Raman signals can be significantly enhanced, with a level up to achieving the single-molecule detection.[4] Due to the sub-wavelength nature of SPs, information or energy can be localized around or transported among nanoscale structures without suffering from the diffraction limits of light. Therefore, the control of SPs forms the fundamental basis for the cutting-edge researches in plasmonics, for which potential applications have been widely found in biomedical sciences, energy harvesting and information technology.[2,5–11]

In this review article, we briefly introduce our recent progress in research on the control and application of surface plasmons. In Section 2, we present a direct design methodology called surface wave holography and discuss its application to plasmonic wavefront manipulation for SPP transport in planar plasmonic structures. In Section 3, we discuss surface plasmon amplification in metallic nanostructures with gain, both theoretically and experimentally. In Section 4, we discuss microscopic and macroscopic manipulation of fluorescent radiation from gold nanorod hybrid structures. In Section 5 we summarize this paper.

*Project supported by the National Basic Research Program of China (Grant Nos. 2013CB632704 and 2013CB922404), the Knowledge Innovation Program of the Chinese Academy of Sciences (Grant No. KJCX2-EW-W02), and the National Natural Science Foundation of China (Grant Nos. 11104342 and 11374357).

†Corresponding author. E-mail: jiafangli@aphy.iphy.ac.cn

‡Corresponding author. E-mail: lizy@aphy.iphy.ac.cn

© 2014 Chinese Physical Society and IOP Publishing Ltd

2. Surface wave holography for plasmonic wavefront manipulation

Subwavelength structures on a metallic surface have attracted much interest over the years.[12] Many extraordinary properties occur when modulating the metallic surface with subwavelength structures.[12–14] When a subwavelength aperture is surrounded by periodic corrugations, the transmitted light can emerge as a beam with a small angular divergence, instead of diffracting in all directions.[14] This finding has opened a path to achieve a high level of h energy collection without losing the subwavelength resolution. Following this development, many structures have been proposed to realize and utilize the focusing and collimation of light on a corrugated metallic surface.[15,16] It is believed that the interaction between a surface electromagnetic wave and subwavelength metallic structures on the surface plays a key role in the focusing and beaming phenomenon.[13,16,17]

In this section, by introducing the concept of surface wave holography,[18–20] we show that the extensively studied focusing and beaming structures,[14,16] metallic films with a hole surrounded by grooves etc., are essentially a plane hologram.[18–21] The surface wave holography method can be readily employed for wave-front shaping of near-infrared light through a subwavelength hole, as well as designing holographic plasmonic lenses for surface plasmons with a complex wavefront profile.

2.1. Introduction of surface wave holography

Surface wave holography (SWH) is an approach that incorporates the concept of conventional holography into the regime of surface electromagnetic waves; for example, the SPPs.[20] It involves the writing and reading processes of the object wave with the aid of the reference wave. However, unlike conventional optical holography, the reference wave is now a confined plasmonic wave that is excited by illumination of the aperture and which propagates outwards away from the aperture, instead of the usual plane wave. Moreover, the major purpose of this approach is not to record object information in the plasmonic nanostructure but to provide a direct design methodology to determine plasmonic nanostructures to implement certain functionalities of plasmonic wavefront shaping and manipulation (set as desired object waves) with no need for complicated inverse-problem solution in electromagnetics.

As shown in Fig. 1, the SWH involves three major steps, which are: the writing process, the hologram sample fabrication process, and the reading process. First, the phase distribution of the objective wave U_0 is extracted as $\phi_0(x,y)$. The writing surface wave U_w (reference wave) excited by the subwavelength hole has a phase of $\exp(\mathrm{i}nkr)$, where n is the effective index of surface wave, k is the wave number in vacuum, and $r=(x^2+y^2)^{1/2}$. Here we choose $n \approx n_{SPP}=\sqrt{\varepsilon_1\varepsilon_2/(\varepsilon_1+\varepsilon_2)}$, where ε_1 is the permittivity of air and ε_2 the permittivity of silver. In this step, the groove positions can be determined with coordinates satisfying $[-\phi_0(x,y)]-nkr=2m\pi$ (m is an integer), which can be flexibly accomplished with FDTD simulation without solving complex inverse problems. In the second step, the grooves and the central hole are fabricated with focused ion beam lithography. The typical scales for both the depth and width of the grooves are chosen to be around $\lambda/10$, so that the change of phase is negligible when the surface wave passes a groove.[22] In the final reading process, an incident light is shone from the back side of the grooves (for convenience, we define the face with grooves as the front face, and the one without grooves as the back). Because of the deep subwavelength scale of the hole, surface waves are excited at the front surface[22] and scattered by the grooves when propagating outwards from the hole. Since the grooves are placed in designed positions, due to the interference of the scattered waves, a designed pattern of field distribution can be made to appear at a given position at the front side; that is, the "object" is read out. It can be seen that this SWH methodology is very simple to operate and use. In addition, it has wide applicability in both the pre-designated object wave profile and the surface reading and writing wave profile. As a result, this method can become a universal direct design tool for plasmonic nanostructures that implement certain functionalities of plasmonic wavefront shaping and manipulation.

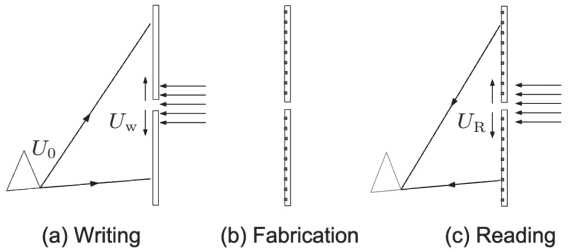


Fig. 1. Schematic of surface wave holography.[22] (a) Writing process. U_0 is the objective wave and U_w is the writing reference wave. The grooves are designed at positions where the superimposed phase of U_0 and U_w equals $2m\pi$ (m is an integer). (b) Fabrication process. The grooves and the central hole are fabricated at designed positions. (c) Reading process. An incident light is shone from the back side of the grooves and the reading wave U_R, which is equal to the writing reference wave U_w, is excited by the central hole and scattered by the grooves. The interference of the scattered waves reconstructs the "object".

2.2. Wavefront shaping of near-infrared light through a subwavelength hole

The behavior of light passing through a small hole in an opaque screen is an old subject in fundamental optics. It is well known in geometrical optics that a pinhole can form an inverted image on the opposite side, as a consequence of the rectilinear propagation of light rays. When the hole is shrunk to a dimension comparable with wavelength, light manifests its

wave nature and shows a diffracted pattern.[23] If one further decreases the radius of the hole to $r \ll \lambda$, it is predicted that when light passes through such a hole in a perfectly conducting and infinitely thin metal film, the wave is diffracted in all directions and the transmission efficiency is weak and proportional to $(r/\lambda)^4$.[24] However, a famous experiment performed by Ebbesen and coworkers showed that if a subwavelength aperture in a metal film is surrounded by periodic grooves, the transmitted light can emerge as a beam with a small angular divergence, instead of being diffracted to a wide angular range.[14] It is believed that the interaction between the surface electromagnetic wave (called surface plasmonic wave) and the subwavelength metallic structure plays a key role in this phenomenon.[17] Since then, beaming and focusing effects existing above or on a corrugated metallic surface[16] have been added to the answer to this old question. On the other hand, with the development of near-field optics and the invention of various nano-scale lasers, such as the quantum cascade laser[25] and the very-small-aperture laser,[26] the knowledge of light passing through a subwavelength hole and the manipulation on the transmitted wave front have drawn much attention.[27,28]

In a previous paper, we showed that SWH allows one to directly shape the surface corrugation structure of a metal film to realize a given functionality of electromagnetic wave transport with no need to solve complex inverse problems. We have made use of the methodology to demonstrate that a 1064-nm beam passing through a 180-nm-radius hole surrounded by well-designed grooves can appear in the pattern of a Latin letter "L" or "O" at a given position.[29]

Specifically, assume that we expect an "L" pattern field distribution to appear at 10.64 μm (here the concerned wavelength is 1064 nm) above the front surface when the light is shone through the hole. First, we use the FDTD method to calculate the propagation of an "L" source, as shown in Figs. 2(a) and 3(a). The "L" source is placed at z=10.64 μm, and the propagating field at 10.64 μm away, i.e., z=0 plane, is stored as U_0. Then, we extract the phase distribution of the x component of the electric field of U_0, and denote it as $\phi_0(x,y)$. The writing surface wave excited by the subwavelength hole has a phase as $\exp(ikr)$. According to Ref. [22], we can get grooves at positions $[-\phi_0(x,y)] - kr = 2m\pi$, where m is an integer. In the specific operation, we divide the $z = 0$ plane into a number of 30 nm×30 nm square pixels (in accordance with the grid used in FDTD simulation), and introduce a criterion $|\phi_0(x,y) + kr - 2m\pi| \leq 0.25$ to determine which pixel should be etched.

With the above information, we fabricate our "L" hologram sample, whose scanning electron microscopy (SEM) picture is shown in Fig. 3(a2). A 240-nm-thick silver film is sputtered onto an SiO_2 substrate, and the grooves and the central hole are fabricated with focused ion beam lithography. The depth of these grooves is about 0.10 μm, while the widths depend on their positions. Obviously, the structure shown in Fig. 3(a2) is aperiodic and is even not closed curves. The "reading" of the structure in Fig. 3(a2) is first performed by using FDTD. As shown in Fig. 3(a3), an intensity pattern of the "L" shape can be recognized clearly, accompanied with some undesirable ripples, for which the minimum resolution of the imaging system is about one wavelength.

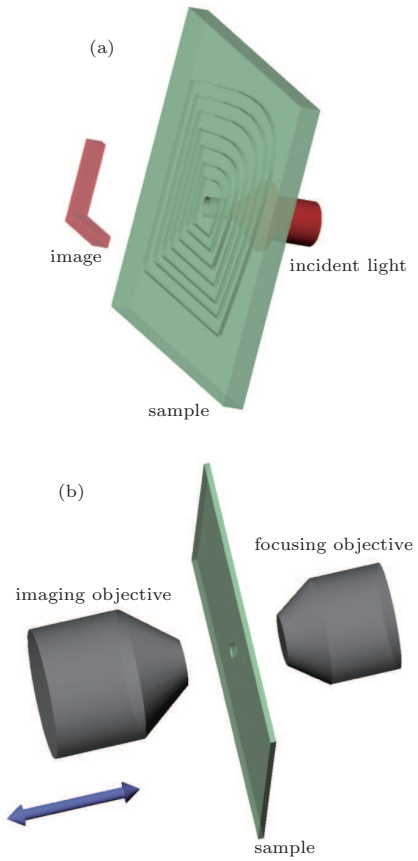


Fig. 2. (a) Schematic diagram of wave manipulation of light through a subwavelength hole drilled in an optically opaque silver thin film. The subwavelength hole is surrounded by a series of shallow, narrow grooves. An incident light, such as a circular polarized plane wave, is shone from the back side of the silver film, and a complex pattern, such as a letter "L" appears in a given position. (b) Experimental setup. A focusing objective is used to get a high intensity incident wave at the back side, and an imaging objective can move forward and backward at the front side in order to see the field distribution at different heights.[29]

For experiments, as shown in Fig. 2(b), we mount an imaging objective to a high-precision translation stage to monitor the field distribution at various heights. When the focal plane of the imaging objective is moved from the back side to front side, a clear image of the hole is first detected, and then a bright "L" shaped pattern gradually appears. Taking the plane where the image of the hole is the clearest as the $z = 0$ plane, we obtain the clearest image of "L" after moving the imaging objective 14.1±0.7 μm above, which is a little far from our designed height (10.64 μm). Two factors might contribute to

this deviation. The first is the quite large image depth of "L", which ranges from 10 μm to 13 μm, as shown in Fig. 3. The second is the finite focal depth of the imaging objective, about 1 μm (one wavelength), which makes the determination of the $z = 0$ plane and the imaging plane not precise enough. As another example, figures 3(b1)–3(b4) show the counterparts of an "O" pattern. Strictly, according to the steps described above and using an "O" source to write the structure on the silver surface, we reconstruct the "O" image in both simulation and experiment. The simulated "O" appears between $z = 10$ μm and $z = 13$ μm, and the z value for the clearest "O" picture in experiment is 14.5±1.2 μm.

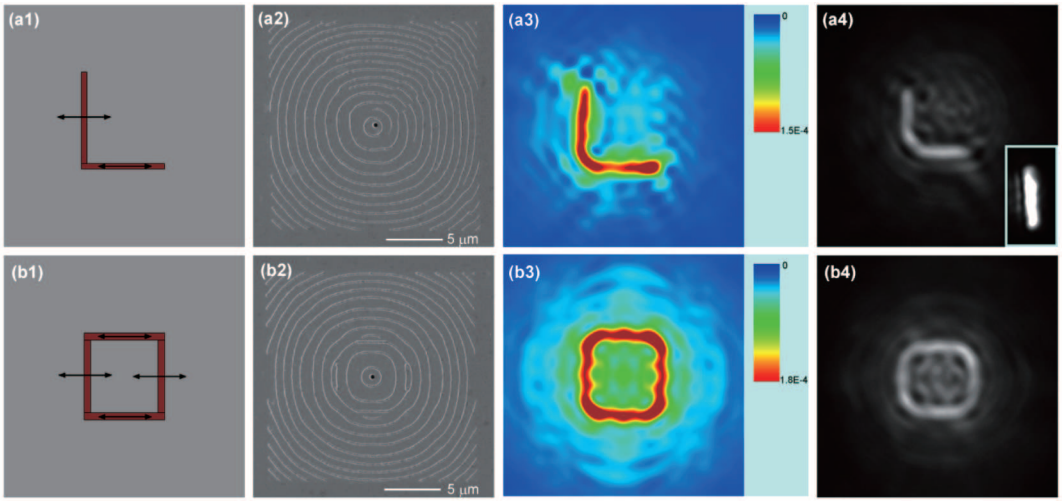


Fig. 3. (a1) and (b1) Patterns we used to calculate U_0 in FDTD simulations. (a2) and (b2) SEM pictures of the fabricated hologram samples ((a2) for "L" and (b2) for "O"). (a3) and (b3) FDTD-simulated xy-plane field distributions at 10.64 μm above the front faces of the samples ((a3) for "L" and (b3) for "O"). The calculated range here is 18×18 μm^2 for both samples. (a4) and (b4) Experimental photos at the clearest positions ((a4) for "L" and (b4) for "O"). The inset of (a4) is the image of a 6×1 μm^2 blank strip of the same silver film, acting as a ruler for our imaging system.[29]

So far, we have shown that near-infrared light passing through a subwavelength hole in a 240-nm-thick silver film can be manipulated to form a shape of "L" and a shape of "O" by carving appropriate patterns of grooves on the outgoing surface according to the SWH method. Such surprising results indicate that, contrary to common expectation, the wave through a subwavelength hole on a thin opaque metal film is quite sensitive to the surface details. The SWH method enables us to achieve complicated transport wavefront engineering functionalities in three-dimensional (3D) space, especially in, but not limited to, the Fresnel region, where the conventional optical elements behave poorly, by merely fabricating two-dimensional surface structure. We expect that such a concept can find applications not only in holography[20] and plasmonic structures design,[22] but also in sensing, information storage, and so on.

2.3. Holographic plasmonic lenses for SPs with complex wavefronts

Plasmonic nanostructures can be exploited to fulfill and model conventional optical transport control functionalities, but at a much smaller size, providing an ultracompact integration solution for the exploitation of micro-size and nano-size optical devices. For example, light collimators,[3,14] plasmonic wave plates,[30] lenses,[16,31] and focusing[17] have been designed to manipulate light waves above a metallic surface in the Fresnel region.

In this paper, we show yet another successful example of employing the SWH methodology to design a plasmonic lens that can focus light transmitted through an aperture of complicated geometric shape (other than a simple circular subwavelength aperture) in an opaque metal screen. It has been well known for some years that milling grooves on the outgoing surface of a metal film can focus and collimate light emerging from a subwavelength hole.[14,16] As an application, Capasso's group integrated these structures on the output surface of semiconductor lasers and greatly reduced the light-emitting angular divergence.[3] The prospect of integrating plasmonic structures to shape the output beams of semiconductor lasers was therefore expected, and was demonstrated in Ref. [3]. However, up to now these findings were limited to apertures of the simplest shapes; that is, a narrow slit which was treated as a line, and a tiny hole which was treated as a point. For the case of a slit, the structure was usually taken as a two-dimensional (2D) case and only the light confinement along the short axis could be realized. In this paper, we show that the light from a slit, which is usually treated as a 2D structure, can also be confined in three dimensions.[32] In other words, we can use

a specially designed plasmonic lens to achieve 3D focusing of light transmitted through such a slit on a spot. With this exotic lens placed at the exit plane of a semiconductor laser, the ordinary output slit beam can be shaped into a 3D focusing spot in the Fresnel zone.

In our experimental demonstration,[32] we have built these plasmonic samples with their surface morphology of grooves perforated on a silver thin film directly determined according to the SWH method, and the 632.8-nm light emerging from a slit (11×0.12 μm^2) can be focused to a point located at 7 μm above the silver surface by these plasmonic lenses. In detail, a silver film with a thickness of 240 nm is deposited on a SiO_2 substrate (with a refractive index of 1.55) by magnetron sputtering, and then patterned by focused ion beam lithography. By controlling the dwell time of the focused ion beam milling, only the hole is penetrable, and the grooves are approximately 80 nm deep. An SEM picture of the fabricated sample is shown in Fig. 4(a). Usually, such a slit is treated as a 2D case in practice because the length is two orders of magnitude larger than the width. However, it can be seen in Fig. 4(b) that the surface waves excited by an 11 μm×0.12 μm slit in a bare smooth silver film has a complex distribution, and this makes shaping the wavefront into a 3D focusing spot a very difficult task in the framework of traditional inverse problem solution, which would require very complicated and time-consuming electromagnetic computations. Yet, we show that it is an ordinary process in the framework of SWH to deal with these complex surface waves, showing the great advantage of this direct method.

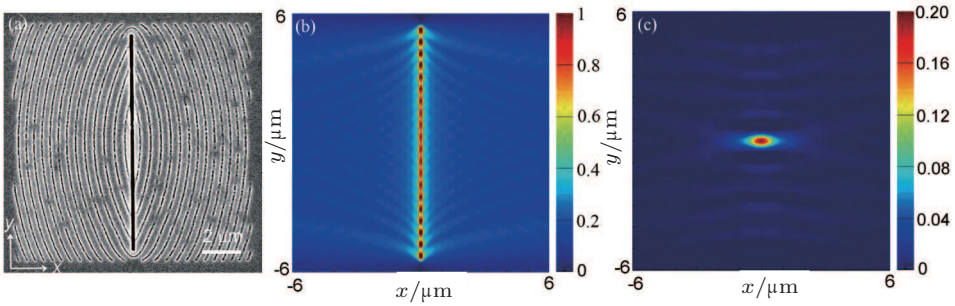


Fig. 4. (a) An SEM photo of the slit sample. The measured size of the slit is 11.10 μm×0.15 μm. (b) The simulated field distribution of the surface waves excited by an 11μm×0.12 μm slit. Note that the silver surface in (b) is not patterned with grooves. (c) The simulated field distributions at $z = 7$ μm above the patterned slit sample. The calculated intensities in panels (b) and (c) are normalized to the incident wave intensity.[32]

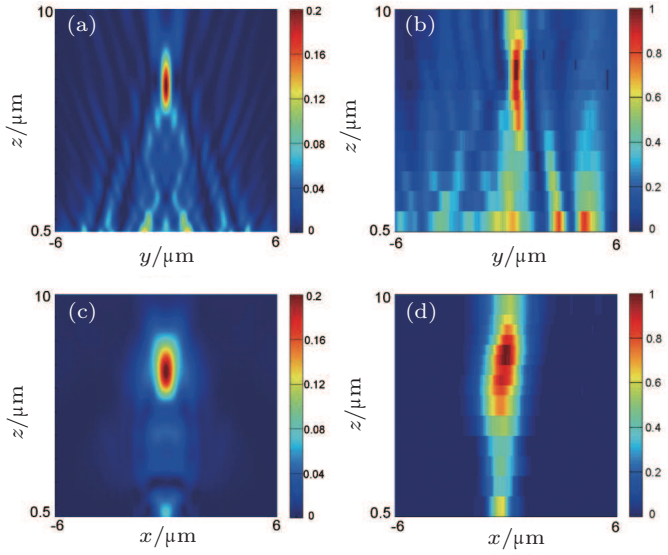


Fig. 5. Field evolutions in the z direction. (a) Simulated and (b) experimental field distributions in the yz plane ($x = 0$). (c) Simulated and (d) experimental field distributions in the xz plane ($y = 0$). In the simulated figures (a) and (c), the calculated intensities are normalized to the incident waves, while the intensities shown in the experimental figures (b) and (d) are normalized by the divided-by-maximum method.[32]

According to our design, if we illuminate the patterned sample in Fig. 4(a) with a 632.8-nm laser from the side without grooves (the side where $z < 0$), a focal spot located at (0, 0, 7) μm is expected. This is indeed confirmed by our FDTD simulation results, as shown in Fig. 4(c). To provide more insight into this focusing effect, the field evolutions in the z direction, that is, the field images at the yz plane ($x = 0$) and the xz plane ($y = 0$), are shown in Fig. 5. In the simulation results displayed in Figs. 5(a) and 5(c), a rice-shaped hot spot with its maximum intensity at $z = 6.7$ μm is clearly recognized, which fits quite well with our design ($z = 7$ μm).

In experiment, in order to monitor the focusing effect of the structure, we use a scanning near-field optical microscope (SNOM), whose probe aperture is approximately 100 nm, to scan the field distributions at different heights above the sample surface. The sample is fixed in a stage that can move precisely in the z direction, so that the SNOM probe, which scans the signals at a fixed plane, can give the field distributions at different heights. As the probe moves outward from the surface, as shown in Figs. 5(b) and 5(d), a focus is found at $z = 7.5$ μm, which is slightly different from the simulated value (6.7 μm). This difference is attributed to the deviation of the fabricated structure from the simulated structure, espe-

cially the deviation in the width of the slit, whose value in the fabricated sample is 0.15 μm, whereas in the simulation it is 0.12 μm. These rice-shaped maxima in Fig. 5 indicate that the focusing depth of the fabricated structure is approximately 2.5 μm, which is relatively large when compared with the full-width at half maximum (FWHM) of the focus. A good agreement between the experimental results and the simulated results confirms the focusing effect of the holographic plasmonic lens and again confirms the power of the SWH method in handling complicated wavefront shaping problems.

3. Surface plasmon amplification in metallic nanostructures with gain

The nanoscale confinement nature of SPs serves as the fundamental platform for wide applications of plasmonics. Its most notable feature is the field-enhancement effect, which is attributed to strong plasmon-matter interaction. Take the nanoparticle-based plasmon–molecule nanosystem for example.[33,34] On the one hand, for molecules coated around the metal nanoparticles, the strongly enhanced local electric field can enhance the excitation efficiency of fluorescence. Meanwhile, a coupling to SPs causes an increase in the local density of optical states (LDOS), inducing an increase in the radiative emission rate of the molecules. On the other hand, for the SPR of the metal nanoparticles, the gain obtained from the fluorescent molecules can compensate the ohmic losses occurring during the strong oscillations of conducting electrons. Once the energy transferred from gain media to SPs overcomes the energy dissipation of the SPR, tremendous amplification of the SPR can occur, opening a new regime for plasmonic nanolasers.[35–37]

In this paper, we will first present our numerical simulations of surface plasmon amplification in gold nanoparticles with gain and our development of an all-analytical semiclassical theory of spaser performance in a plasmonic nanocavity. Then, we will discuss our experimental studies of amplified spontaneous emission of SPPs at the interface between a silver film and a polymethyl methacrylate (PMMA) film doped with dye molecules.

3.1. Surface plasmon amplification in gold nanoparticles with gain

Gold nanorods (GNRs)[38] are cylindrical nanoparticles that have two axes; that is, the transverse axis (along the short axis) and the longitudinal axis (along the long axis). The anisotropic shape of GNRs induces a splitting of the SPR into transverse and longitudinal SPR modes,[39] in contrast with the single SPR mode of nanospheres. Compared with isotropic gold nanoparticles like gold nanoshells[40] and nanospheres, GNRs have small sizes and large optical cross sections at the longitudinal SPR wavelength, which is widely tunable in the visible to near-infrared wavelength range[39] when changing the aspect ratio; that is, the ratio of the long axis' length to the short axis' length. Therefore, GNRs have been demonstrated to have potential in applications ranging from biological imaging, sensing and photothermal therapy to optical data storage, fluorescence enhancement, plasmonic coupling devices, etc.

The large optical cross sections but small volumes make GNRs a desirable candidate for the realization of surface plasmon amplification effects; that is, 'spaser' (surface plasmon amplification by stimulated emission of radiation).[41] Since this concept was proposed by Stockman *et al.* in 2003,[42] many methods have been advanced to realize lasing spaser systems.[35–37] One effective method is to utilize the interaction between metallic nanoparticles and gain media. For example, gold nanospheres (GNS),[37] gold nanocubes,[43] and concentric spherical nanoparticles[35] incorporated with gain materials have been explored for the generation of spaser-like phenomena. However, the lasing wavelength of spherical spaser-based nanolasers is limited by the narrow band and weakly tunable SPR wavelength of the GNS over the size variation. By utilizing the strong longitudinal SPR of GNRs, we have shown that GNRs are more efficient for building an active nanosystem for spaser with unique wavelength tunability and polarization sensitivity.[41]

As illustrated in Fig. 6(a), the proposed active nanosystem based on GNRs is composed of GNRs encapsulated by a silica shell doped with gain media. Such nanocomposite particles can be synthesized by an aqueous solution-based method.[33] In calculations, the core-shell particle is exposed in air with a refractive index $n_0 = 1.0$ and the refractive index of the shell is set as $n_{\text{shell}} = 1.5 - \mathrm{i}k$. Here the "gain coefficient" k, which is related to the amplification coefficient of light intensity via $g = 4\pi k/\lambda$,[43] is introduced to describe the interaction strength between the incident light and the gain media. Under such a condition, the optical cross sections of extinction (C_{ext}), scattering (C_{scat}), and absorption (C_{abs}) for the GNR-based nanosystem are calculated with different gain coefficients, using the discrete-dipole approximation (DDA) method.[43] It is found that C_{ext}, C_{scat}, and C_{abs} vary sensitively with k and there is a critical value of $k_{\text{c}} = 0.0312$, where C_{ext} at the SPR wavelength nearly reaches the value of zero. At this critical point, as shown in Fig. 6(b), the absorption cross section becomes negative with an extremely high absolute value ($\sim$600 μm^2), which indicates that a strong SPR amplification occurs. Under this condition, the peak value of C_{scat} reaches an extreme value of about 600 μm^2, which is about 7×10^4 times the value when $k = 0$, as plotted in Fig. 6(c). Meanwhile, the SPR linewidth is significantly compressed by two orders of magnitude. The value of k_{c} can be called the "threshold" for building up strong amplification of SPR.

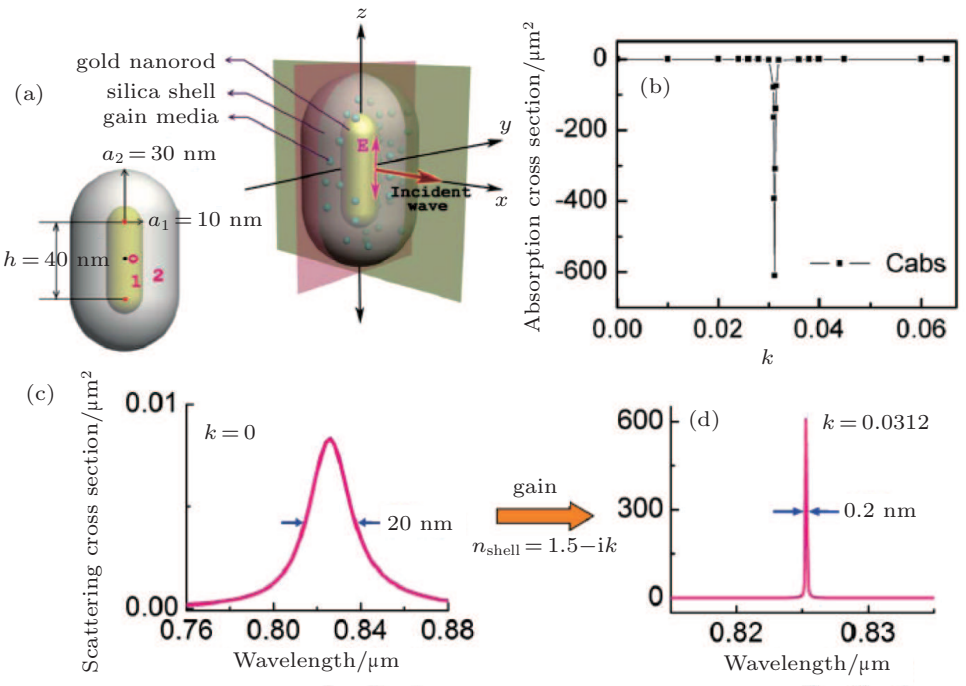


Fig. 6. (a) Schematic diagram of the GNR-based active nanosystem. (b) Calculated absorption cross section at the SPR wavelength of GNR as a function of gain coefficients (k). The spaser threshold is identified at $k = 0.0312$. (c) Calculated scattering cross section spectra for the nanosystem with different k values. At the spaser threshold, the scattering cross section is enhanced by a factor of $\sim 7 \times 10^4$, and the linewidth is compressed by two orders of magnitude.[41]

Compared with the core-shell GNS, the threshold of the core-shell GNR system is nearly one order of magnitude lower, and at the spaser state the absolute magnitude of the scattering cross section or absorption cross section of the GNR-based system (~ 600 μm^2) is more than 150 times larger than that of the system (~ 3.8 μm^2). Therefore, it can be inferred that it is much easier to realize spaser or great amplification of SPR by taking GNR (rather than GNS) as the basic structure of the core-shell active nanosystem. The low threshold of the gain coefficient in this case poses more options for suitable gain materials, such as dye molecules, rare-earth ions, and semiconductor quantum dots. Moreover, it is found that by using the GNR-based nanosystem, the center wavelength of spaser can be widely tuned from visible to near-infrared range by changing the aspect ratio of the GNRs. In this way, a flexible, wavelength-tunable spaser of nanometer scale is possible.

Surface plasmon amplification effects achieved with active metal nanosystems also provide intriguing power to enhance local electric field intensity to a level where single-molecule detection by surface-enhanced Raman scattering (SERS) can be readily achieved. For a theoretical demonstration, we employed a cubic Au nanobox with a gain material encapsulated in the core, as illustrated in Figs. 7(a) and 7(b).[43] The complex refractive index of the core medium is set at $1.33 - \mathrm{i}\kappa$ where κ_{core} is introduced as the gain coefficient of the core medium. The outer and inner edge lengths of the Au nanobox are 40 and 32 nm, respectively, with the thickness of all six walls being 4 nm. Such nanostructures can be easily synthesized using the galvanic replacement reaction between single-crystal Ag nanocubes and $HAuCl_4$.[44] The SPR peaks of these nanoboxes can be conveniently tuned from the visible to the near-infrared region, in particular with strong absorption at a wavelength around 800 nm for biomedical applications, such as early cancer diagnosis and photothermal treatment.[44]

Electric-field patterns calculated with the DDA method[45] show that at the resonant wavelength of 779.2 nm a huge enhancement of local field intensity occurs at the high-field spots ("hot spots") of the nanobox. For example, with $\kappa_{\mathrm{core}} = 0.143$, the average field intensity at the front surface is at a high level of 1.0×10^8, whereas the field intensity at the four hot spots can reach 2.4×10^8, as shown in Fig. 7(c). This means that the SERS enhancement factor (G factor) over the entire front surface area of the active nanosystem can be as high as 1.0×10^{16}, a level that has not been reached by other types of metal nanoparticles. This happens because a significant resonance occurs at the gain level, as shown in Fig. 7(d). It can be seen that at $\kappa_{\mathrm{core}} = 0.143$, the scattering cross section is enhanced to 845 μm^2, or 1.6×10^4 times the value of a passive Au nanobox, and the overall amplification cross section is also greatly enhanced to 854 μm^2, which is 5×10^4 times the value of the passive counterpart (with $\kappa_{\mathrm{core}} = 0$). Meanwhile, the overall extinction cross section is a negative value, which means that the nanosystem can amplify the incident light although scattering along all directions is quite strong. All these features clearly indicate the initiation of lasing.

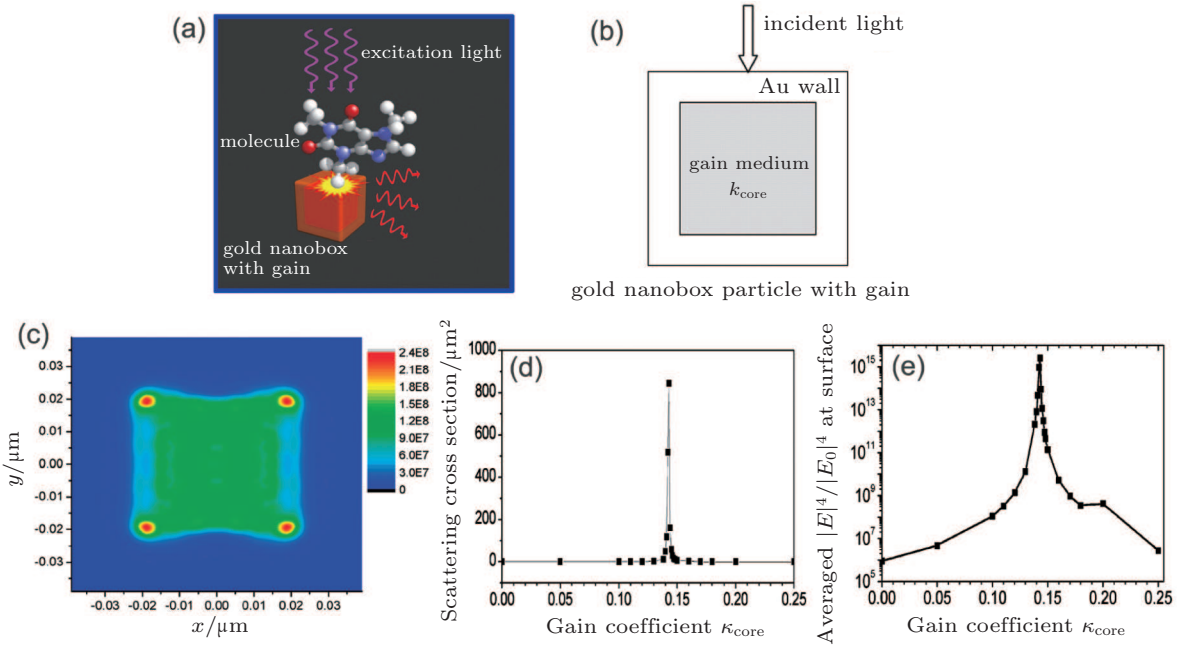


Fig. 7. (a) Schematic of the gold nanobox with gain for SERS application. (b) Schematic of the gold nanobox containing a gain medium with gain coefficient κ_{core} in the core. (c) Calculated local electric field intensity at the front surface for a cubic Au nanobox with a gain material of $n = 1.33 - 0.143i$. Excitation wavelength: 779.2 nm. (d) Resonant optical scattering cross sections of the nanobox as a function of κ_{core} at an excitation wavelength of 779.2 nm. Maximum light–particle interaction occurs at $\kappa_{core} = 0.143$, where the scattering cross section is over 2×10^4 times the value for a Au nanobox containing no gain material and the amplified cross section is 4×10^6 times the value for a same-size cubic nanoparticle of the pure gain material. (e) Averaged SERS signal at the surface of the particle as a function of the gain coefficient κ_{core} at a resonance wavelength of 779.2 nm.[43]

It should be mentioned that in practical single-molecule detection it is difficult to locate only a single molecule in the "hot spot" region. It is, therefore, more interesting to see if the overall SERS G factor on the entire surface area of a metal nanoparticle can reach a sufficiently high level. Figure 7(e) shows that in the narrow window of κ_{core} from 0.140 to 0.145, the average surface G factor exceeds 1.0×10^13. Although the average G factor is one order of magnitude lower than in the surface "hot spots", the surface area is at least two orders of magnitude larger than the area of these "hot spots". As a result, the overall possibility to observe single molecule Raman signal is much higher when one utilizes the entire surface rather than only the "hot spot" region. In this regard, the current active nanosystem is very promising for realizing single-molecule detection in a single nanoparticle via the SERS technique. At the critical point of $\kappa_{core} = 0.143$, the average surface field intensity enhancement factor is about 2.8×10^7 while the average G factor is at a very high level of 2.5×10^{15}. This means that in this condition the active nanosystem has a great potential for single-molecule detection by SERS.

The giant enhancement of local electric field intensity can be simply understood by connecting field intensity and the energy accumulation capability of the plasmonic nanocavity. When gain is introduced to the gold nanobox, the linewidth of the SPR peak is drastically reduced, as the gain will compensate for the loss due to metal absorption, and the Q factor is three orders of magnitude greater than in passive particles. This means that the photonic energy will accumulate within the active cavity for a much longer time before it is dissipated. As a result, the optical field intensity, which is just proportional to the photon energy density, becomes strongly enhanced, leading to an even more gigantic enhancement of the SERS factor.

3.2. All-analytical semiclassical theory for a spaser nanosystem

Experimental approaches to manipulate light–matter interaction at the nanoscale level have advanced quickly in recent years, leading to the generation of spaser in plasmonic nanocavities.[35–37,41,43] However, a well-understood analytical theory to quantitatively explain certain characteristics of the spaser system is yet to be found and is greatly needed. In the above section, we have theoretically shown that surface plasmons can be amplified by introducing gain media into metallic nanoparticles. At a critical value of the gain coefficient, the linewidth of SPR peaks is drastically reduced, implying the ignition of laser in this active nanophotonic system. However, in this study, the role of gain medium is described by a phenomenological parameter called gain coefficient k, and therefore, the study is in the framework of pure classical electromagnetics. To have a fully quantitative understanding of light–matter interaction in these active plasmonic nanocavities incorporating gain media made from dye molecules or

other materials, the quantum nature of the gain medium must be fully taken into account.

We have recently developed an all-analytical semiclassical theory to investigate the energy exchange between active materials and fields, and evaluate the spaser performance in a plasmonic nanocavity.[46] The plasmonic nanocavity is composed of a metallic core (providing plasmon resonance modes) surrounded by a dielectric shell containing active materials (providing gain), as schematically illustrated in Figs. 8(a) and 8(b). The active materials are described by a general four-level atomic system and the structure can describe the gain and loss process happening in a general optical nanocavity very well. Specifically, when electrons are pumped from the ground-state level with a constant pump rate, spontaneous emission happens immediately. The feedback effect of the SPR of the metallic core will cause stimulated emission to continue until a steady state is reached. The schematic diagram of the atomic system is shown in Fig. 8(c), where levels 1 and 2 are the lower and upper lasing levels, respectively. Under the dipole approximation, the active materials can be seen as dipoles. Our aim is to develop a methodology to describe the characteristics of light–matter interaction in this nanolaser system. Similar to conventional laser theory, we consider atomic transitions in the current nanolaser system quantum mechanically and adopt the model of atomic rate equations to describe these transitions, while classically handling the radiation of electromagnetic field, the motion of which follows Maxwell's equations. The interaction between atoms and fields is thus treated semiclassically. Such a semiclassical theory should yield a much more precise description and better prediction of the optical properties of these nanolaser systems than the usual classical theory, in which the role of the atoms comprising the active materials is described by the phenomenological parameter of dielectric permittivity.[41,43]

This theory incorporates the four-level atomic rate equations in association with the classical oscillator model for active materials and Maxwell's equations for fields, thus allowing one to uncover the relationships among many factors, including the characteristics of the spaser (output power, saturation, and threshold), the nanocavity parameters (quality factor, mode volume, loss, and spontaneous emission efficiency), atomic parameters (number density, linewidth, and resonant frequency), and external parameters (pumping rate). This semiclassical theory has been employed to analyze previous spaser experiments and shows that using a single gold nanoparticle plasmonic nanocavity to ignite the spaser is very difficult due to spaser's high threshold. This theory can be commonly used in understanding and designing all novel microlaser, nanolaser, and spaser systems.

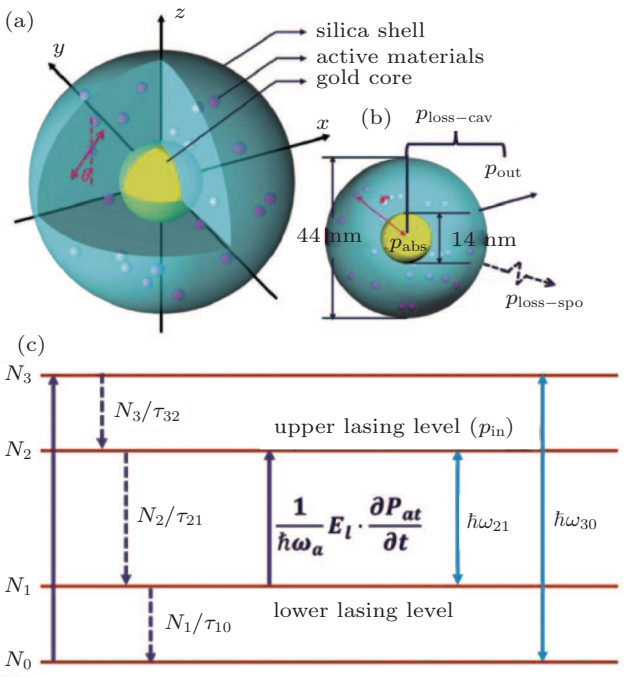


Fig. 8. Schematic plot of the light–matter interaction of a general four-level atomic system with a metallic nanocavity.[46] (a) Geometry of the plasmonic nanocavity, which is a core-shell nanoparticle consisting of a metallic core and dielectric shell doped with four-level atoms as active materials. Each atom is modeled as a radiation dipole. θ is the angle of the dipole polarization, and r is the distance between the dipole and the center of the metallic core. (b) Energy output from the plasmonic nanocavity, where p_{out} is the output laser power density, p_{abs} is the metallic absorption power density of the plasmonic cavity, and $p_{\mathrm{loss-spo}}$ is the loss of spontaneous emission power density. (c) Schematic of a general four-level atomic system that describes the spontaneous and stimulated radiation and various atomic transition parameters. The straight and dashed lines correspond to the radiative and nonradiative transitions, respectively. p_{in} is the storage power density by the upper lasing level.

3.3. Experimental observation of amplified spontaneous emission of SPPs

Plasmonic structures can impose strong enhancement and confinement on electromagnetic field, which finds applications ranging from sensing, sub-wavelength resolution imaging, plasmonic circuitry, etc.[47] However, the intrinsic absorption of metal fundamentally limits the performance of these plasmonic systems; for example, the sensitivity of SPR to external perturbations.[48] Integrating metallic structures with an optical gain medium has been proposed as a possible solution to this problem in versatile schemes, based on which surface plasmon amplification has been successfully demonstrated.[49–53] However, the direct observation of the amplification effect of SPPs by gain media is still challenging and is beset with various ambiguities and has aroused controversies. The reason lies in the difficulties of direct recognition of SPPs' spontaneous emission (SE), amplified spontaneous emission (ASE), and lasing-like stimulated emission (LSE), as well as the direct photonic emission from the gain medium.

To solve this puzzling problem, we have conducted

experiments based on a typical Kretschmann configuration (see Fig. 9(a)).[54] When pump pulses (wavelength 532 nm, pulse width $\sim$ 5 ns, and repetition rate 0.5 Hz) strike the PMMA/Rh6G film, the SPP modes are excited in two ways: the fluorescence of Rh6G can be scattered into SPPs by the roughness of the surface, while the excited Rh6G molecules near the metal surface can be directly coupled into SPP modes with a high efficiency via a nonradiative decay process. Once SPPs are excited, they propagate along the interface of silver and PMMA/Rh6G, and are simultaneously decoupled into radiative waves by the prism at an angle that satisfies $\sqrt{\varepsilon}_1 \sin\theta = \sqrt{\varepsilon_2\varepsilon_3/(\varepsilon_2+\varepsilon_3)}$, where ε_i $(i = 1,2,3)$ is the permittivity of the i-th medium as marked in Fig. 9(a). The angle-dependent decoupling of SPPs can be utilized to resolve the emission of SPPs from the direct photon emission of Rh6G. As shown in Fig. 9(a), we use two detection paths, D1 and D2, to realize this function. In D1, an optical fiber (400 μm in diameter) connected to a spectrometer (Ocean Optics, USB2000) is used to collect the SPP emission at the prism side with different detection angles (θ) and pump intensities (I_P). While in D2, the direct photon emission from Rh6G that is not coupled to SPPs is detected from the film side.

Figure 9(b) shows the SPP emission spectra at a fixed angle $\theta = 58.4^\circ$ under different I_P. A shoulder at about 592.87 nm can be recognized, and it grows much faster than the other part of the spectra when I_P increases. This spectral evolution is mostly like the ASE properties that are involved with gain amplification.[55] In our system, there are only two possible amplification mechanisms, which are: the amplification of Rh6G emission from the PMMA/Rh6G film[55] and the amplification of SPPs propagating along the metal/dielectric interface.[56] In such a case, to identify the type of ASE in Fig. 9(b), we record the Rh6G photon emission spectra at the D2 path under the same I_P. As illustrated in Fig. 9(c), although the SE intensity of Rh6G grows with the increased I_P, no significant change occurs in the spectral shape. Therefore, it can be concluded that the ASEs observed in Fig. 9(b) are from the amplified SPPs. These results provide a clear physical picture of the SPPs amplified by gain media.[54] It turns out that the phenomenon reported in Ref. [53] may actually be an ASE instead of the LSE of SPPs.

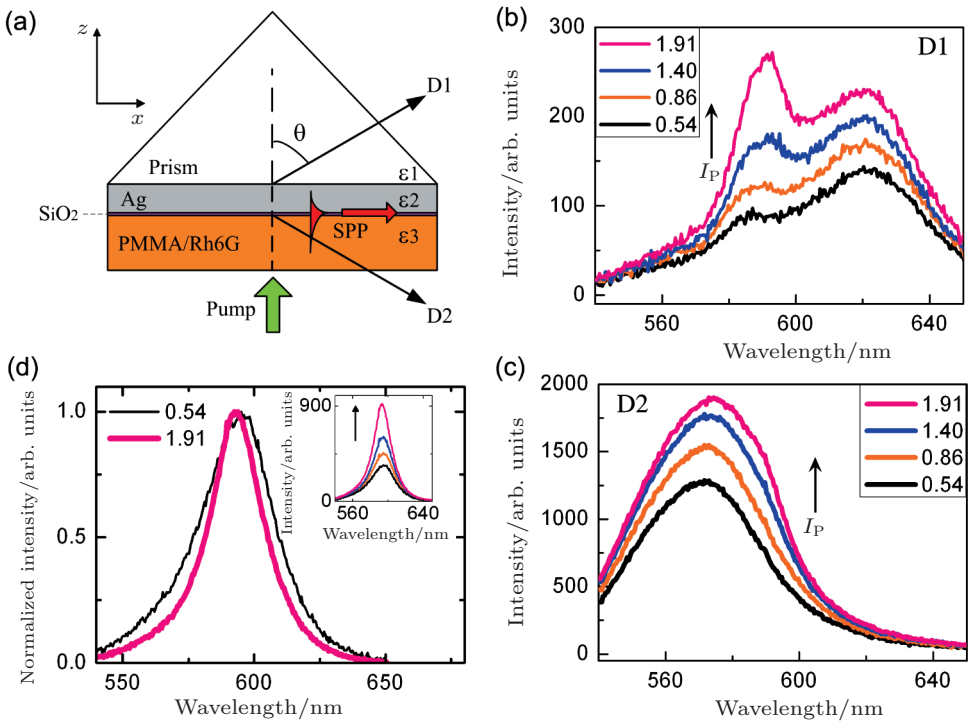


Fig. 9. (a) Schematic of the prism-based experimental setup for observing SPP amplification. SPPs are decoupled by the prism and corresponding emission is measured through detection path D1. Emission of Rh6G is measured from the film side through detection path D2. (b) ASE spectra of SPPs decoupled at $\theta = 58.4^\circ$ with different I_P as noted (in unit of mJ/cm^2). $\lambda_{ASE} = 592.87$ nm. (c) Measured emission spectra of Rh6G recorded at D2 under the same I_P as in panel (b). (d) Normalized emission spectra of SPPs decoupled at $\theta = 59.2^\circ$. Inset: measured emission spectra of SPPs under different I_P. From bottom to top: $I_P = 0.54$, 0.86, 1.40, and 1.91 mJ/cm^2.[54]

Moreover, it is expected that the introduction of gain will compensate the dissipation losses and, therefore, narrow down the SPP emission spectra. This has been confirmed by our experiments, as shown in Fig. 9(d), and by some other work.[51] In the same way, it is naturally expected that the introduced gain could also improve the performance in the angular re-

sponse of the plasmonic system; that is, narrow down the angular response of the SPP emission. However, in a recent experimental study we observed unusual effects.[57] As plotted in Fig. 10(a), at some wavelengths, the angular distribution of the SPP emission shows nearly no change when the pump intensity I_p increases from 0.54 to 1.91 mJ/cm^2. While in a certain wavelength range, the FWHM is unusually broadened with increased pump intensity. For example, at the ASE_{SPP} peak wavelength 592.87 nm, the FWHM increases from 1.11° to 1.31° when I_p grows from 0.54 to 1.91 mJ/cm^2 (see Fig. 10(b)). To find out the trend of the unusual angular broadening, the wavelength-dependent response of the angular FWHM on increased pump intensity is further illustrated in Fig. 10(c). Two features are worth pointing out. Firstly, at low pump intensity, the FWHM drops gradually with wavelength as an overall trend. Secondly, it is only in the range of 582–600 nm (see the gray region in Fig. 10(c)) that the FWHM is increased with the increase in I_p. Most interestingly, the gray region in Fig. 10(c) is located within the ASE_{SPP} spectral region, which implies that the net gain (as manifested by the existence of ASE_{SPP}) broadens the angular distribution of SPP emission rather than making it narrower. These observations indicate that, although theoretical work can predict the generation of spaser,[57] there are still many non-classical phenomena that need to be explored and understood.

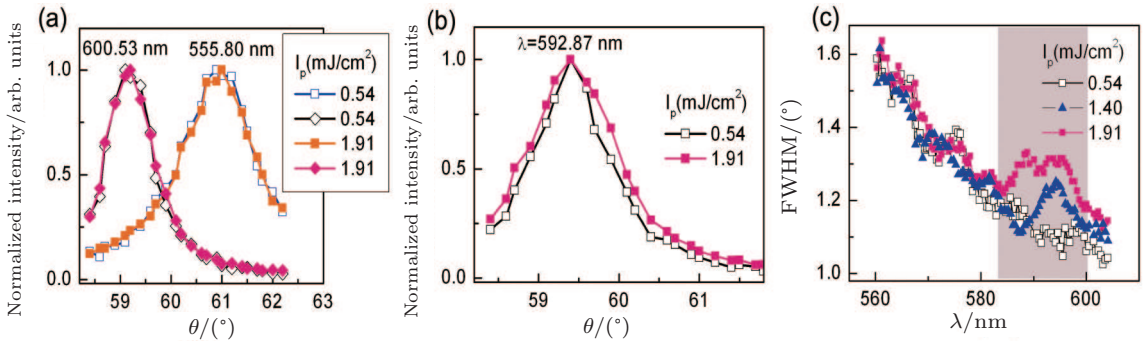


Fig. 10. (a), (b) Angular distribution of SPP emission at 555.80, 600.53, and 592.87 nm under different I_p. (c) FWHM of the angular distribution of SPP emission as a function of the detection wavelength under different I_p. The gray shading indicates the region where the FWHM is unusually increased.[57]

4. Manipulation of fluorescent radiation from GNR hybrid structures

Metal nanoparticles exhibit fascinating plasmonic properties with potential applications ranging from bioscience, catalysis and sensing to information technology such as imaging and storage. The excitation of localized SPR in metal nanoparticles results in nanoscale confinement of electromagnetic fields near the metal surface and a significant enhancement in the local density of optical states.[5] Such properties have been widely employed to study the interactions between plasmons and fluorophores, such as fluorescence enhancement[33] and the realization of nanolaser.[49]

In this section, we first present our recent study on the microscopic manipulation of fluorescence from dye molecule-coated GNRs. A double-SPR fluorescence enhancement mechanism is proposed and demonstrated with a single GNR hybrid nanoparticle. Then, we demonstrate macroscopic manipulation of group GNR hybrid nanostructures by means of a simple but efficient film-stretch method and realize polarized emission with such a macroscopic film.

4.1. Fluorescence enhancement assisted by double SPRs of GNRs

With regard to plasmon-enhanced fluorescence, there are two kinds of enhancement mechanisms: excitation enhancement and emission enhancement.[34,59] Although one can realize either excitation enhancement or emission enhancement by utilizing the single SPR of some metal nanoparticles, plenty of experiments have shown that, in the case of the maximum 'excitation–emission' efficiency, the SPR wavelength lies right between the peak excitation wavelength and peak emission wavelength of the emitters, as schematically illustrated in Fig. 11(a).[60] Such compromised phenomena are also commonly seen in SERS experiments.[2] The very essence of this phenomenon is that the 'excitation–emission' efficiency η of fluorescent molecules is related simultaneously to the excitation efficiency γ_{Ex} and the emission efficiency γ_{Em},[61] which can be simply described as $\eta = \gamma_{Ex} \times \gamma_{Em}$. The excitation wavelength of lasers and the emission wavelength of fluorescent molecule are described as λ_{Ex} and λ_{Em}, respectively. When the SPR wavelength of the metal particle satisfies the relation $\lambda_{SPR} = \lambda_{Ex}$, the highest excitation efficiency is

achieved; that is, $(\gamma_{Ex})_{max}$. While at $\lambda_{SPR} = \lambda_{Em}$, the highest emission efficiency is achieved; that is, $(\gamma_{Em})_{max}$. However, generally, since $\lambda_{Em} \neq \lambda_{Ex}$, if λ_{SPR} matches one of the wavelengths, the other must be mismatched. Therefore, $(\gamma_{Ex})_{max}$ and $(\gamma_{Em})_{max}$ cannot be accomplished simultaneously. While if $\lambda_{Ex} < \lambda_{SPR} < \lambda_{Em}$, the linewidth of the SPR spectrum can encompass both of the excitation and emission bands of fluorescent molecules and thus results in an optimized but compromised 'excitation–emission' efficiency η_{Com}. Obviously, $\eta_{Com} < (\gamma_{Ex})_{max} \times (\gamma_{Em})_{max}$.

We recently proposed a scheme to further increase the 'excitation–emission' efficiency.[58] By matching the double SPR wavelengths (transversal SPR (TSPR) and longitudinal SPR (LSPR) modes) with the excitation and emission wavelengths, respectively, one can realize $(\gamma_{Ex})_{max}$ and $(\gamma_{Em})_{max}$ simultaneously and achieve $\eta_{max} = (\gamma_{Ex})_{max} \times (\gamma_{Em})_{max}$. This proposed idea is implemented by using a GNR that has two SPR modes, as shown in Fig. 11(b).

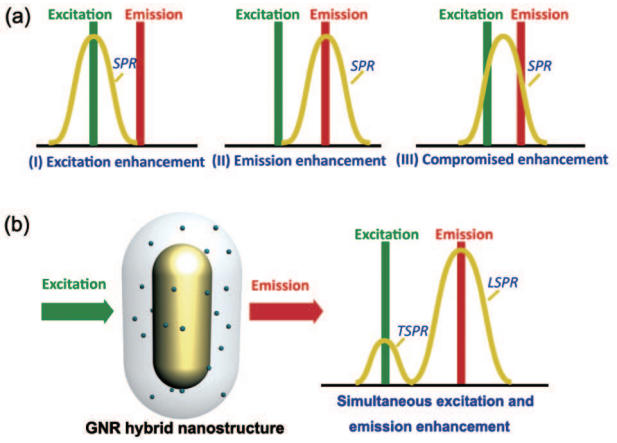


Fig. 11. Schematic models of the fluorescence enhancement mechanisms assisted by the SPR of metal nanoparticles.[58] (a) Excitation enhancement (I) and emission enhancement (II) are realized by matching the single SPR wavelength with the excitation and emission wavelength, respectively. Optimized but compromised enhancement (III) is generally achieved by overlapping the single SPR band with both the excitation wavelength and the emission wavelength. (b) Simultaneous enhancement of both excitation and emission by utilizing the TSPR mode of gold nanorods to enhance the excitation possibility, while the LSPR mode is used to enhance the emission rate.

For experimental demonstration, we use hybrid nanostructures composed of GNRs or a GNS in the core and oxazine-725-doped silica in the shell, which have been utilized for studies of plasmon-enhanced fluorescence and plasmon–molecule interactions.[34] Since previous studies showed that the fluorescence can be chemically quenched when fluorophores are located very close (< 5 nm) to the metal surface,[34] the thickness of the silica shell in our studies is chosen to be around 20 nm, with which a net fluorescence enhancement can be measured. To test the proposed fluorescence enhancement effects induced by the double SPRs of GNRs, wavelength matching is critical. To avoid an overlap between the excitation wavelength of laser and the emission band of the molecules, the excitation wavelength is chosen at 532 nm, which is outside the emission band of oxazine-725 (ranging from 600 nm to 800 nm).

To compare the fluorescence enhancement induced by the different mechanisms depicted in Fig. 11, three types of nanoparticles are deposited onto indium tin oxide (ITO) glass slides, as shown by the SEM images in Fig. 12. Three single nanoparticles are chosen from each type: 1) GNS1, which has single SPR wavelength matched with the excitation wavelength (532 nm); 2) GNR1, whose TSPR and LSPR wavelengths are matched with the excitation wavelength and emission band of oxazine-725, respectively; 3) GNR2, which has no SPRs matched with either the excitation wavelength or with the emission band. In order to measure the scattering and emission from exactly the same single nanoparticles, a combined dark-field (DF) scattering and photoluminescence characterization system is employed. The measured fluorescence spectra of GNS1, GNR1, GNR2 and oxazine-725 molecules in solution are plotted in Fig. 12(d), in which all spectra are recalculated to equivalently show the corresponding emission from the same amount of 1000 fluorophore molecules. One can clearly see that GNR1, which has double SPRs matched with both excitation wavelength and emission band, has the strongest fluorescence. Compared with the emission from the same amount of dye molecules in solution, the peak fluorescence intensity from GNR1, GNS1, and GNR2 is enhanced by 20.8, 5.3, and 4.5 times, respectively.

The enhanced emissions from GNR samples are confirmed by conducting time-resolved experiments with a time-correlated single photon counting (TCSPC) system. Figure 12(e) shows the measured fluorescence intensity decay of oxazine-725 in silica composite, GNS shell (with SPR wavelength at ~550 nm) and GNR shell (with LSPR wavelength at ~ 700 nm), of which the resolved lifetimes are 2.51, 1.46 and 0.72 ns, respectively. The shortest lifetime, of oxazine-725 molecules in a GNR shell, indicates that the emission rate at the LSPR wavelength is greatly enhanced, which is physically caused by the increased local density of optical states around the GNR due to the existence of LSPR. It should be mentioned that here the decrease in lifetime is not as great as the increase in peak fluorescence intensity (Fig. 12(d)) because the measured fluorescence intensity decays in Fig. 12(e) are from the whole emission band of oxazine-725 rather than only at the peak wavelength.

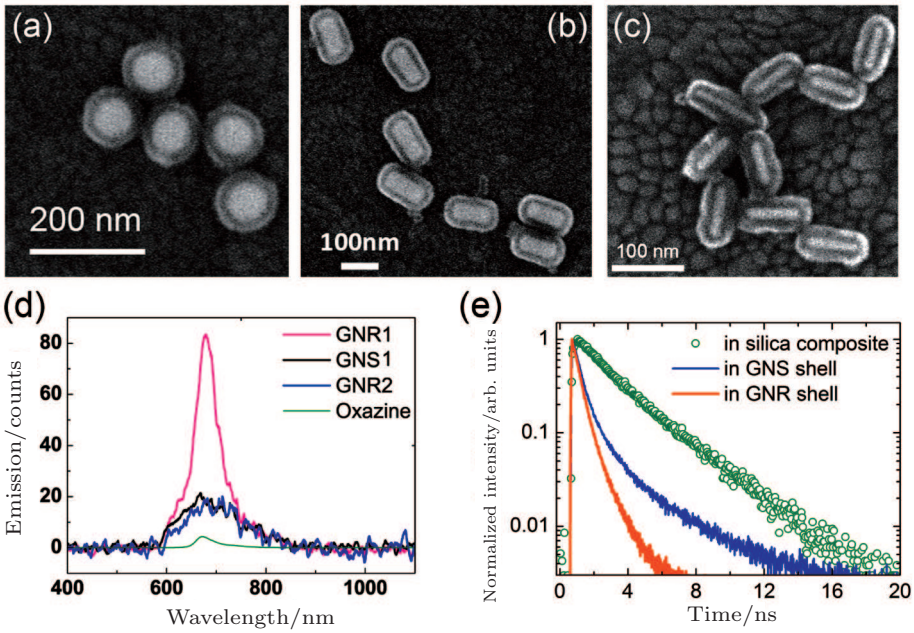


Fig. 12. (a)–(c) SEM images of core-shell GNS and two types of GNRs on ITO glass slides. (d) Fluorescence emission spectra (from top to bottom) of GNR1, GNS1, GNR2, and oxazine-725 water solution. The spectra are recalculated from direct measurements and equivalently show the emission from the same amount (1000) of dye molecules in each sample. (e) Measured fluorescence intensity decays of oxazine-725 molecules in different samples. It can be seen that fluorescence intensity decays much faster in the GNR sample than in other samples.[58]

So far, we have proposed and demonstrated an effective scheme to enhance fluorescence by utilizing the double SPR modes of GNRs. In this scheme, the excitation probability of the dye molecules is first enhanced by the local electric field enhancement due to the TSPR of the GNR. Then, the emission rate at the LSPR wavelength is further enhanced by the increased local densities of optical states around GNR due to the existence of LSPR. By experimentally employing GNRs coated with dye molecule-doped silica shell, maximal fluorescence enhancement is obtained when the TSPR and LSPR wavelength of GNR are well matched with the excitation wavelength and emission band of dye molecules, respectively. Our scheme has opened up a new way to enhance fluorescence or SERS signals by fully utilizing the multiple SPRs of plasmonic nanostructures.

4.2. Macroscopic control of fluorescence from GNR hybrid structures

The studies of single metallic nanoparticles have aroused great interest, due to their direct insight into various macroscopic plasmonic properties from a nanoscale point of view, such as plasmonic absorption, scattering, emission and field localization.[40,45] The applications of single nanoparticles include surface-enhanced Raman spectroscopy, single molecule detection, fluorescence enhancement, etc.[33,34,43,59,62] However, single nanoparticles are normally smaller than 100 nm and are difficult to manipulate by conventional methods. Therefore, applications of metallic nanoparticles are mainly based on assemblies in which the nanoparticles are randomly distributed.[8,9,63] This causes an averaging issue in the case of anisotropic nanoparticles in that the anisotropy is always replaced by a macroscopically isotropic format. For example, while the emission from a single hybrid GNR nanoparticle has strong polarization effects,[33,34] the assembled nanostructures cannot preserve these anisotropic properties due to the averaging effect of the random distribution and orientation of nanoparticles.

Recently, we demonstrated that macroscopic polarized light emission can be simply realized by aligning anisotropic hybrid GNR nanoparticles.[64] Moreover, by fully utilizing the LSPR of the hybrid GNRs, the relative excitation–emission efficiency of the macroscopic film can be enhanced by ~ 15 times when both the excitation and emission polarization directions are along the stretching direction. These studies provide a simple but important method for the realization of polarized emission, as well as the easy applications of active anisotropic nanoparticles.

The hybrid GNR nanoparticles in our experiments are composed of GNRs in the core and dye molecule (oxazine-725) doped silica in the shell (as shown in Fig. 12(b), purchased from Nanoseedz). For sample preparation, we use a film-stretch method to align GNR metal particles.[39] Specifically, the GNR nanoparticles are purified and mixed with a 15% aqueous PVA solution with a volume ratio of 1:1. GNRs/PVA films are prepared by pouring the mixture into a Petri dish and then drying the samples naturally for 24 hours

at room temperature, which results in uniform polymer films with a thickness of ~ 100 μm (depending on the amount of the mixture used). Finally, the GNRs/PVA films are cut into rectangular segments that are manually stretched in one direction under heating at ~ 65 °C (as schematically shown in Fig. 13(a)) until a desired length is obtained. In our experiments, the final length of the stretched film is chosen to be ~ 5 times its original length, which ensures nearly complete alignment of the GNRs inside the stretched films,[39] as characterized by the SEM images displayed in Fig. 13(b).

During the stretch process, the PVA molecules elongate along the stretch direction, which orients the longitudinal axes of GNRs along the stretch direction.[65] Because the LSPR mode is inherently polarized along the longitudinal axis, the stretched films will show collective LSPR when the incident light is polarized parallel to the stretch direction. In such a way, the stretched film could macroscopically enact the anisotropic optical properties of a single GNR. As shown in Fig. 13(c), a stretched GNRs/PVA film shows distinct colors when the incident light is polarized parallel and perpendicular to the stretch direction, respectively, while the original film shows the same color in both polarization directions. These color displays are inherently associated with the corresponding absorption spectra. As shown in Fig. 13(d), the original film shows two absorption peaks irrespective of the light polarization directions (curves I and II). After the stretch, the film possesses only one absorption peak upon each polarized excitation, which corresponds to the LSPR (curve III) and TSPR (curve IV), respectively. This splitting of the LSPR and TSPR in the macroscopic films could find useful applications in polarization-dependent color display devices.[38]

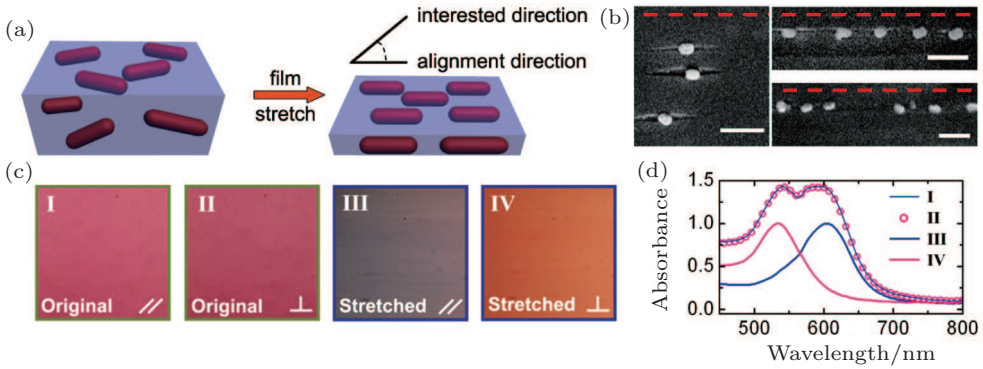


Fig. 13. (a) Schematic illustration of the film-stretch process, by which the randomly distributed hybrid GNRs are aligned with the long axis along the stretching direction. (b) SEM images of hybrid GNRs in stretched PVA films. After the stretch, most of the hybrid GNRs in the film are aligned with the long axis along the stretching direction (indicated by dash lines). Scale bars are 500 nm.[64] (c) Optical microscope images of the original and stretched GNRs/PVA film under white light illumination with polarization parallel (∥) and perpendicular (⊥) to the stretch direction. (d) Measured absorbance spectra of the GNRs/PVA films corresponding to (c).[39]

To study the emission properties of the stretched macroscopic film with aligned hybrid GNRs, the sample is first excited with a circularly polarized pump at wavelength of 633 nm. It is found that when varying the angle of the detection polarization ($\alpha_{\rm det}$), the measured emission spectra show strong anisotropy. To avoid the cut-off effects of the long-pass filter, the emission intensity at the LSPR wavelength of 742 nm is monitored. As shown in Fig. 14(a), the emission intensity of the stretched sample varies periodically and can be well fitted using a cosine squared function together with an exponential decay that occurs when the detection polarization angle is continuously increased. This decay in intensity is due to the laser-induced photo-bleaching effects.[33] After calibrating the exponential decays, one can clearly see the dipole-like pattern in the polar plot of Fig. 14(b), which indicates an emission polarization close to linear polarization. By comparison, the emission from the original film shows only an exponential decay in Fig. 14(a), which is fully isotropic after calibration of the exponential decay (see Fig. 14(b)). It should be mentioned that this polarized emission from the stretched film is not only observed at the wavelength of 742 nm but also seen at other wavelengths ranging from 650 to 880 nm. Therefore, the stretched macroscopic film could be useful for applications such as converting circularly polarized light into broadband linearly polarized emission, as depicted in Fig. 14(c).

Our further studies with linearly polarized excitation ($\theta_{\rm ex}$) while varying the angle of the detection polarization ($\alpha_{\rm det}$) show that the measured emission spectra are highly dependent on the values of $\theta_{\rm ex}$ and $\alpha_{\rm det}$, as plotted in Fig. 14(d), where the symbols "∥" and "⊥" denote the angles of 0° and 90^o, respectively. For example, $I_{\parallel\,\parallel}$ means that the spectrum is measured when both the excitation and emission polarization directions parallel to the stretching direction (i.e., $\theta_{\rm ex} = 0°$ and $\alpha_{\rm det} = 0°$), while $I_{\perp\,\parallel}$ means that the spectrum is measured

when $\theta_{ex} = 90^\circ$ and $\alpha_{det} = 0^\circ$. To compare the fluorescence efficiency among different experimental schemes, the relative excitation–emission efficiencies of the sample are calculated by normalizing the fluorescence spectra to the spectrum of $I_{\perp\,\parallel}$. As shown in Fig. 14(e), the highest relative efficiency ($\sim$15) is achieved when both the excitation and emission polarization directions are parallel to the stretching direction. Both figures 14(d) and 14(e) clearly demonstrate that to obtain the maximum polarized fluorescence from the stretched samples, the selection of both excitation and emission polarization is critical. The difference between the maximum ($I_{\parallel\,\parallel}$) and minimum ($I_{\perp\,\parallel}$) emission intensity can be as high as 15 times. The underlying physics for is that when both the excitation and emission wavelengths are within the LSPR band of hybrid GNRs, the excitation rate is increased, due to the local field enhancement, and the emission rate is enhanced by the increased local density of optical states when the LSPRs are excited at both the excitation and emission wavelengths. Therefore, both excitation and emission enhancement are induced, and the maximum excitation–emission efficiency for fluorescence is achieved.

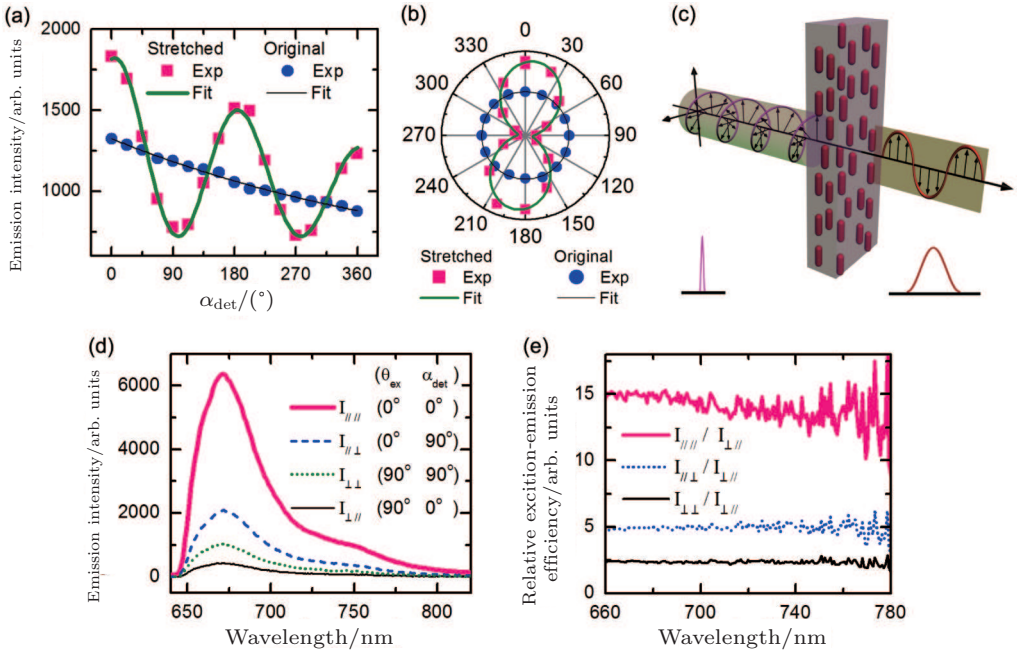


Fig. 14. (a) Measured emission intensity at wavelength 742 nm versus detection polarization angle (α_{det}) under excitation with circular polarization for the original and stretched film. The data are fitted with a cosine squared function together with an exponential decay. (b) Polar plot of the experimental and fitted data in panel (c) after calibrating the exponential decays. (c) Illustration of the applications of the stretched hybrid GNRs for converting circularly polarized light into broadband linearly polarized emission. (e) Measured emission spectra of the stretched film with different θ_{ex} and α_{det}. The symbols "$\parallel$" and "$\perp$" denote the angles of 0^o and 90°, respectively. The first and second subscripts represent the values of θ_{ex} and α_{det}, respectively. (e) Relative excitation–emission efficiency of the emission spectra shown in (d).[64]

5. Conclusions

In summary, we have introduced some of our recent work on manipulation of SPs for potential applications, specifically for the control of plasmonic wavefront and light–matter interaction in metallic nanostructures. We have briefly introduced the principles of the SWH methodology and shown that SWH allows one to directly determine the surface corrugation structure of a metal film to realize a given functionality of electromagnetic wave transportation without the need to solve complex inverse problems of electromagnetics. As examples, we have presented the wave-front shaping of near-infrared light through a subwavelength hole in an opaque screen, as well as holographic plasmonic lenses for SPs with complex wavefronts, both of which have been successfully designed and realized experimentally. We have explored various efficiently ways to manipulate and harness light–matter interaction in metallic nanostructures. In particular, we have theoretically investigated SP amplification in gold nanobox and nanorod particles incorporating gain media and found that the linewidth of SPR in these active nanosystems can be drastically reduced, and the local electric field intensity can be significantly increased, leading to a giant enhancement of the SERS factor up to a level exceeding the single-molecule detection limit. We have presented an all-analytical semiclassical theory that incorporates four-level atomic rate equations for gain media and Maxwell's equations for optical field to eval-

uate the physics and performance of a nanolaser made from a plasmonic nanocavity. We have then presented experimental studies on amplified spontaneous emission of SP polaritons at the metal/gain medium interface by adopting a standard prism setup. Finally, we have discussed experimental demonstration of both microscopic and macroscopic manipulation of fluorescence from dye molecules. We have shown that a double-SPR mechanism can be adopted to enhance the fluorescence signal of dye molecules in hybrid GNR nanoparticles with appropriate geometric parameters. We have also presented a simple polymer film-stretching technique to align group hybrid GNR nanoparticles so that the whole macroscopic film behaves the same way as a single microscopic nanoparticle. In addition, the manipulation of light radiation, such as adjusting the polarization and intensity, can be achieved in such an active GNRs embedded macroscopic thin film. The studies presented in this review not only provide fundamental ideas for sophisticated nanoscale manipulation of SPs but also hold potential for applications in areas such as optical displays, biomedical sensing, information integration and transportation, energy harvesting, etc.

Acknowledgments

The authors would like to thank Prof. Guo Hong-Lian, Dr. Gan Lin, Miss Liu Si-Yun, Huang Lu, Zhong Xiao-Lan, Liu Ju, Mr. Chen Yu-Hui, Wang Ben-Li, Wang Chen, and Li Qiang for their useful contributions.

References

[1] Hutter E and Fendler J H 2004 *Adv. Mater.* **16** 1685
[2] Willets K A and Van Duyne R P 2007 *Ann. Rev. Phys. Chem.* **58** 267
[3] Yu N F, Fan J, Wang Q J, Pflugl C, Diehl L, Edamura T, Yamanishi M, Kan H and Capasso F 2008 *Nat. Photon.* **2** 564
[4] Chen K H, Hobley J, Foo Y L and Su X D 2011 *Lab Chip* **11** 1895
[5] Hu M, Chen J Y, Li Z Y, Au L, Hartland G V, Li X D, Marquez M and Xia Y N 2006 *Chem. Soc. Rev.* **35** 1084
[6] Huang X H, Neretina S and El-Sayed M A 2009 *Adv. Mater.* **21** 4880
[7] Castaneda M T, Alegret S and Merkoci A 2007 *Electroanalysis* **19** 743
[8] Li X, Lan T H, Tien C H and Gu M 2012 *Nat. Commun.* **3** 998
[9] Zijlstra P, Chon J W M and Gu M 2009 *Nature* **459** 410
[10] Yu N, Genevet P, Kats M A, Aieta F, Tetienne J P, Capasso F and Gaburro Z 2011 *Science* **334** 333
[11] Yu Z Z, Wang Z B, Zhao J M and Jiang T 2013 *Chin. Phys. B* **22** 34102
[12] Ebbesen T W and Genet C 2007 *Nature* **445** 39
[13] Ebbesen T W, Lezec H J, Ghaemi H F, Thio T and Wolff P A 1998 *Nature* **391** 667
[14] Lezec H J, Degiron A, Devaux E, Linke R A, Martin-Moreno L, Garcia-Vidal F J and Ebbesen T W 2002 *Science* **297** 820
[15] Sriturayanich W, Fang N, Sun C, Luo Q and Zhang X 2004 *Nano Lett.* **4** 1085
[16] Lee B, Kim S, Kim H and Lim Y 2010 *Prog. Quantum Electron.* **34** 47
[17] Martin-Moreno L, Garcia-Vidal F J, Lezec H J, Degiron A and Ebbesen T W 2003 *Phys. Rev. Lett.* **90** 167401
[18] Cowan J J 1974 *J. Opt. Soc. Am.* **64** 563
[19] Maruo S, Nakamura O and Kawata S 1997 *Appl. Opt.* **36** 2343
[20] Kawata S, Ozaki M O and Kato J 2011 *Science* **332** 218
[21] Cowan J J 1974 *Opt. Commun.* **12** 373
[22] Chen Y H, Fu J X and Li Z Y 2011 *Opt. Express* **19** 23908
[23] Born M and Wolf E 1999 *Principles of Optics: Electromagnetic Theory of Propagation, Interference and Diffraction of Light*, 7th edn. (New York: Cambridge University Press)
[24] Bethe H A 1944 *Phys. Rev.* **66** 163
[25] Faist J, Capasso F, Sivco D L, Sirtori C, Hutchinson A L and Cho A Y 1994 *Science* **264** 553
[26] Shinada S, Koyama F, Nishiyama N, Arai M, Goto K and Iga K 1999 *Jpn. J. Appl. Phys.* **238** L1327
[27] Yu N F, Wang Q J and Capasso F 2012 *Laser Photon. Rev.* **6** 24
[28] Jun Y C, Huang K C Y and Brongersma M L 2011 *Nat. Commun.* **2** 283
[29] Chen Y H, Huang L, Gan L and Li Z Y 2012 *Light-Sci. Appl.* **1** e26
[30] Drezet A, Genet C and Ebbesen T W 2008 *Phys. Rev. Lett.* **101** 043902
[31] Lin L, Goh X M, McGuinness L P and Roberts A 2010 *Nano Lett.* **10** 1936
[32] Chen Y H, Zhang M Q, Gan L, Wu X Y, Sun L, Liu J, Wang J and Li Z Y 2013 *Opt. Express* **21** 17558
[33] Ming T, Zhao L, Yang Z, Chen H J, Sun L D, Wang J F and Yan C H 2009 *Nano Lett.* **9** 3896
[34] Chen H J, Ming T A, Zhao L, Wang F, Sun L D, Wang J F and Yan C H 2010 *Nano Today* **5** 494
[35] Gordon J A and Ziolkowski R W 2007 *Opt. Express* **15** 2622
[36] Zheludev N I, Prosvirnin S L, Papasimakis N and Fedotov V A 2008 *Nat. Photon.* **2** 351
[37] Noginov M A, Zhu G, Belgrave A M, Bakker R, Shalaev V M, Narimanov E E, Stout S, Herz E, Suteewong T and Wiesner U 2009 *Nature* **460** 1110
[38] Perez-Juste J, Pastoriza-Santos I, Liz-Marzan L M and Mulvaney P 2005 *Coord. Chem. Rev.* **249** 1870
[39] Li J, Liu S, Liu Y, Zhou F and Li Z Y 2010 *Appl. Phys. Lett.* **96** 263103
[40] Oldenburg S J, Averitt R D, Westcott S L and Halas N J 1998 *Chem. Phys. Lett.* **288** 243
[41] Liu S Y, Li J F, Zhou F, Gan L and Li Z Y 2011 *Opt. Lett.* **36** 1296
[42] Bergman D J and Stockman M I 2003 *Phys. Rev. Lett.* **90** 027402
[43] Li Z Y and Xia Y N 2010 *Nano Lett.* **10** 243
[44] Chen J, Saeki F, Wiley B J, Cang H, Cobb M J, Li Z Y, Au L, Zhang H, Kimmey M B, Li X D and Xia Y N 2005 *Nano Lett.* **5** 473
[45] Zhou F, Li Z Y, Liu Y and Xia Y N 2008 *J. Phys. Chem. C* **112** 20233
[46] Zhong X L and Li Z Y 2013 *Phys. Rev. B* **88** 085101
[47] Maier S A 2006 *Plasmonics: Fundamentals and Applications* (New York: Springer)
[48] Piliarik M and Homola J 2009 *Opt. Express* **17** 16505
[49] Noginov M A, Zhu G, Belgrave A M, Bakker R, Shalaev V M, Narimanov E E, Stout S, Herz E, Suteewong T and Wiesner U 2009 *Nature* **460** 1110
[50] Seidel J, Grafstrom S and Eng L 2005 *Phys. Rev. Lett.* **94** 177401
[51] Bolger P M, Dickson W, Krasavin A V, Liebscher L, Hickey S G, Skryabin D V and Zayats A V 2010 *Opt. Lett.* **35** 1197
[52] Ambati M, Nam S H, Ulin-Avila E, Genov D A, Bartal G and Zhang X 2008 *Nano Lett.* **8** 3998
[53] Noginov M A, Zhu G, Mayy M, Ritzo B A, Noginova N and Podolskiy V A 2008 *Phys. Rev. Lett.* **101** 226806
[54] Chen Y H, Li J F, Ren M L, Wang B L, Fu J X, Liu S Y and Li Z Y 2011 *Appl. Phys. Lett.* **98** 261912
[55] Popov O, Lirtsman V and Davidov D 2009 *Appl. Phys. Lett.* **95** 191108
[56] Noginov M A, Zhu G, Mayy M, Ritzo B A, Noginova N and Podolskiy V A 2008 *Phys. Rev. Lett.* **101** 226806
[57] Chen Y H, Li J F, Ren M L and Li Z Y 2012 *Small* **8** 1355
[58] Liu S Y, Huang L, Li J F, Wang C, Li Q, Xu H X, Guo H L, Meng Z M, Shi Z and Li Z Y 2013 *J. Phys. Chem. C* **117** 10636
[59] Li X, Kao F J, Chuang C C and He S L 2010 *Opt. Express* **18** 11335
[60] Chen Y, Munechika K and Ginger D S 2007 *Nano Lett.* **7** 690
[61] Liaw J W and Tsai H Y 2012 *J. Quantum Spectrosc. Rad.* **113** 470
[62] Xia Y N and Halas N J 2005 *MRS Bull.* **30** 338
[63] Gindy M E and Prud'homme R K 2009 *Expert Opin. Drug Del.* **6** 865
[64] Liu S Y, Li J F and Li Z Y 2013 *Adv. Opt. Mater.* **1** 227
[65] Fornasiero D and Grieser F 1987 *Chem. Phys. Lett.* **139** 103